

Calculation of Photoneutron Contamination of Varian Linac in ICRU Soft-Tissue Phantom Using MCNPX Code

Mojtaba Cheraghian, Tayyeb Pourfallah^{1,2}, Amir Abbas Sabouri-Dodaran, Mehrdad Gholami³

Department of Engineering, Payame Noor University, Tehran, ¹Department of Biochemistry, Biophysics and Genetics, Medical College, Mazandaran University of Medical Sciences, ²Department of Medical Physics, Mazandaran University of Medical Sciences, Sari, ³Department of Medical Physics, School of Allied Medical Sciences, Lorestan University of Medical Sciences, Khorramabad, Iran

Abstract

Purpose: The aim of this research was to calculate the fluence, dose equivalent (DE), and kerma of thermal, epithermal and fast photoneutrons separately, within ICRU soft-tissue-equivalent phantom in the radiotherapy treatment room, using MCNPX Monte Carlo code. **Materials and Methods:** For this purpose, 18 MV Varian Linac 2100 C/D machine was simulated and desired quantities were calculated on the central axis and transverse directions at different depths. **Results:** Maximum fluence, DE and kerma of total photoneutrons on central axis of the phantom were 43.8 n.cm⁻².Gy⁻¹, 0.26, and 3.62 mGy.Gy⁻¹, at depths 2, 0.1, 0.1 cm, respectively. At any depth, average of fluence, DE and kerma in the outer area of the field were less than the inner area and in general were about 72%, 52%, and 45%, respectively. **Conclusion:** According to this research, within the phantom; variation of fluence, DE and kerma in transverse direction were mild, and along the central axis at shallow area were sharp. DE of fast photoneutrons at shallow and deep areas were one order of magnitude greater than thermal photoneutrons.

Keywords: ICRU phantom, MCNPX, photoneutron contamination, Varian Linac

Received on: 16-03-2021

Review completed on: 28-04-2021

Accepted on: 29-04-2021

Published on: 07-08-2021

INTRODUCTION

Radiation therapy is an established way for treating cancers. The main challenge in cancer treatment using radiotherapy (RT) is delivering high doses to the tumor volume without harming the healthy tissues.

Unfortunately, despite applying accurate and conform field shape, some unwanted radiation reaches to normal tissues around the tumor and cause damage. This unwanted radiation emerges from scattered photons from photon treatment beam, gamma rays due to produced radionuclides in the treatment room, secondary gamma rays due to inelastic interactions, electron contamination of the treatment beam (i.e. in photon mode) as well as produced neutrons from electronuclear and photonuclear interactions which are named electronutron and photoneutron.

Interactions between high-energy treatment beam and nuclei of constituent minerals of the medical linear accelerator (Linac), beam collimation system, couch, patient's body, air, and walls of treatment room can produce

photoneutrons. Since the threshold energy of (γ, n) reaction for constituent minerals of the head of Linac, such as lead, tungsten, copper, and iron, is generally in the range of 6.74–11.20 MeV.^[1]

Since the quality factor of neutrons is about 2–20 times more than photons,^[2] they have a substantially higher biological effectiveness than photons; therefore, even a small number of neutrons can lead to a nonnegligible effective dose to both patients, in the form of non-target and out-of-field dose, and staff due to activation of in-room materials.^[3] The estimation of photoneutron contamination in RT has been studied by several researchers in various experimental and simulation methods.^[4-10] Bezak *et al.*^[11] and Bezak *et al.*^[12] measured the total dose equivalent (DE) in Rando and water equivalent

Address for correspondence: Dr. Tayyeb Pourfallah,

Department of Biochemistry, Biophysics and Genetics, Medical College, Pyambar Azam Academic Complex, Mazandaran University of Medical Sciences, P.O. Box 48157 33971, Sari, Iran.

E-mail: tpourfallah@gmail.com, tpourfallah@mazums.ac.ir

Access this article online

Quick Response Code:



Website:
www.jmp.org.in

DOI:
10.4103/jmp.JMP_40_21

This is an open access journal, and articles are distributed under the terms of the Creative Commons Attribution-NonCommercial-ShareAlike 4.0 License, which allows others to remix, tweak, and build upon the work non-commercially, as long as appropriate credit is given and the new creations are licensed under the identical terms.

For reprints contact: WKHLRPMedknow_reprints@wolterskluwer.com

How to cite this article: Cheraghian M, Pourfallah T, Sabouri-Dodaran AA, Gholami M. Calculation of photoneutron contamination of varian linac in ICRU soft-tissue phantom using MCNPX code. J Med Phys 2021;46:116-24.

phantoms, using thermoluminescent dosimeter (TLD) and estimated the risk of secondary cancer in organs of Rando phantom in treatment of prostate. Sohrabi and Hakimi measured the dose of thermal and epithermal photoneutrons using a self-made experimental method within a polyethylene phantom.^[13] Bagheri *et al.*^[14] and Bagheri *et al.*^[15] measured the dose of thermal photoneutrons in the treatment of breast cancer within the breast Rando phantom using TLD. Results of these experiments mostly were inconsistent with each other and often with low precision. It seems applying Monte Carlo codes such as MCNPX is more reliable. Barquero *et al.* calculated the effects of total photoneutrons on various organs using MCNP code in a computational phantom.^[16] Many others calculated the spectra of photoneutrons and DE due to photoneutrons in tissue^[17-21] and some of them^[18,22] calculated the DE of fast neutrons in voxel-based phantoms. Calculating the effects of each category of photoneutrons along the beam axis, in water equivalent and water phantoms were conducted by many other researchers.^[5,23-25] Effects of the compensator, pelvic prosthesis, circular cones, grid, and dental restorations were also investigated, too. Investigating the effect of the compensator on photoneutron production was performed using the Monte Carlo MCNPX code and SSNTD CR-39 dosimeter^[26] and calculating the effects of the grid on photoneutrons production was conducted using MIRD phantom.^[4,27,28]

As it is well-known, absorption is the predominant mechanism for losing the energy of thermal neutrons in soft tissue through reactions of $^{14}\text{N}(n, p)^{14}\text{C}$ and $^1\text{H}(n, \gamma)^2\text{H}$. Hence, to consider the role of nitrogen and similarity to the tissue of the body, we used ICRU soft tissue equivalent in simulations. Most of the researchers have studied photoneutrons distribution in the air of the treatment room and only few works studied photoneutrons within the phantom. In addition, previous researches often have reported photoneutrons contaminations in whole or focused to the proportion of fast photoneutrons. In this research, we determined the proportion of thermal (0.001–0.5 eV), epithermal (0.5 eV–0.1 MeV), and fast (0.1–20 MeV) photoneutrons in axial and transverse directions at 159 points of the phantom.

MATERIALS AND METHODS

Simulation

A typical treatment room^[28] with walls, ceiling (thickness of 1.7 m) and floor (thickness of 1 m) from concrete (with density of 2.35 g/cm³ and weight fractions of H 0.6%, O 49.8%, Na 1.7%, Mg 0.3%, Al 4.6%, Si 31.5%, S 0.1%, K 1.9%, Ca 8.3% and Fe 1.2%) simulated [Figure 1].^[27,28] The MCNPX Monte Carlo code, Version 2.6, was applied for simulating the 18 MV Varian Linac 2100 C/D machine [Figure 2]. The head of the Linac including all effective components therein containing the target (W), primary collimator (W), vacuum window (Be), flattening filter (Fe and Ta), ionization chamber (Cu and Kapton), secondary collimator (W and Pb), mirror (Mylar), Jaws (W), and upper circle (Fe) were simulated.

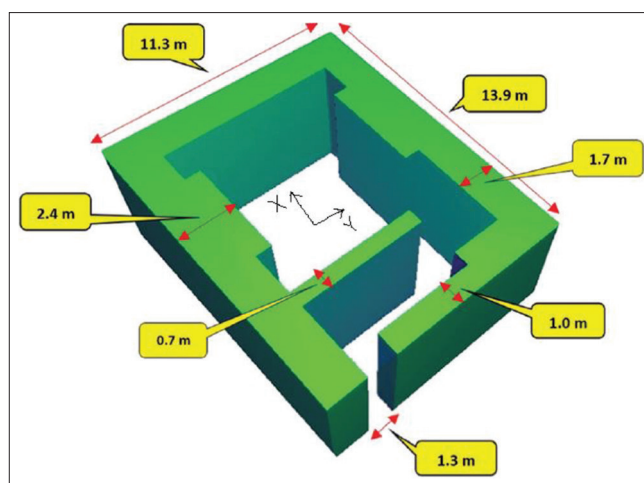


Figure 1: Simulated treatment room^[28]

The source was an electron beam incident on a target made of tungsten and copper and produce Bremsstrahlung photons. Both spatial distribution and energy distribution of the electron beams were considered gaussian, with FWHM of 0.14 cm and FWHM of 1.2 MeV respectively, and the mean energy of electrons set to 18.3 MeV to have the most conformity between measurements and calculations for percentage depth dose and dose profile

Verification of simulation

At first, percentage depth dose and dose profile of the photon beam (set at energy 18 MV, field size 10 cm × 10 cm and source-surface distance [ssd] = 100 cm) were measured by a 0.6 cc Farmer ionizing chamber (PTW Freiburg, Germany) at an IBA Blue Phantom (IBA dosimetry Schwarzenbruck, Germany) with dimensions of 50 cm × 50 cm × 50 cm and constitution of water. For validating the accuracy of simulation, the mentioned parameters were used exactly by simulation. Percentage depth dose (PDD) and relative dose Calculated using *F8 tally and 2×10^9 histories. Energy Cut-off cards were used with values of 0.7 and 0.01 MeV for electron and photon, respectively. For calculating the PDD, voxels' dimensions were set to be 2 cm × 2 cm × 0.2 cm along the central axis (Z-axis) from 0 to 29 cm. For calculating the dose profile, the voxels in the transverse axis (X-axis) had dimensions of $0.4 \times 2 \times 0.4$ cm³ [Figure 3].

Calculation of photoneutron contamination

For calculating photoneutron contamination, ICRU soft-tissue-equivalent phantom (with weight fractions of 10.1% H, 11.1% C, 2.6% N, 76.2% O) with dimensions of 100 cm × 50 cm × 30 cm was simulated [Figures 2 and 4]. In all calculations, the Linac was considered to be in photon mode with 18 MV energy, 10 cm × 10 cm field size and SSD = 100 cm. In these calculations, 2×10^9 electron histories were traced and the relative statistical uncertainties at the majority of points was <10%. To reduce run time, the electron and photon energy Cut-offs were set to be 7 MeV. In Z direction, thickness of the cells were as follows: First cell

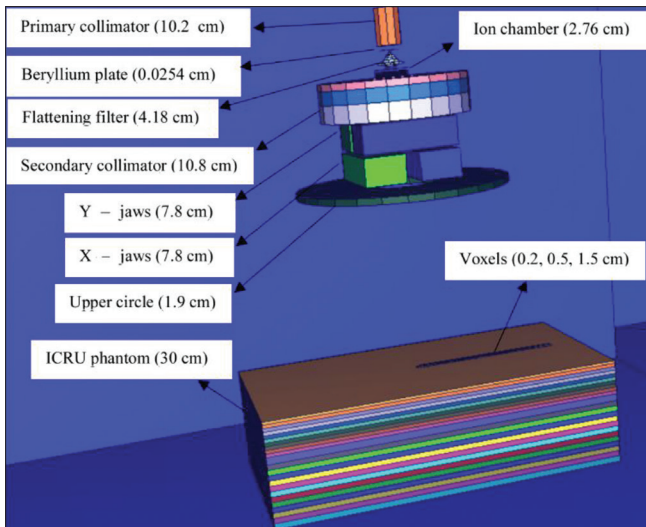


Figure 2: ICRU phantom and different components of the head of 18 MV Varian Linac 2100 C/D. These components were simulated using Visual Editor V22. Dimensions of each component were shown within parentheses

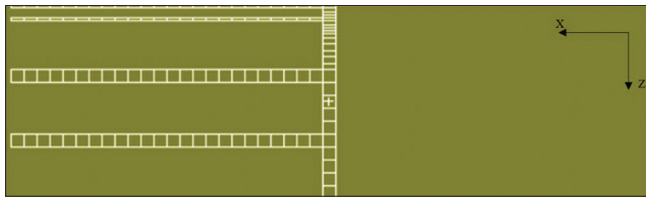


Figure 4: Location of scoring cells in ICRU phantom (side view). The voxels in Z direction were along the central axis of the beam

0.2 cm, from depth 0.2 cm to 10 cm, 0.5 cm and after that 1.5 cm [Figure 4]. Scoring cells considered along the beam axis with dimensions of $1 \times 1 \times (0.2, 0.5, 1.5) \text{ cm}^3$ and at transverse directions $1 \times 2 \times (0.2, 0.5, 1.5) \text{ cm}^3$.

The mode of the simulation was electron-photon-neutron with cross-section libraries of MCPLIB04, EL03, and ENDEF/B-V2 for photon, electron, and neutron, respectively. In the production of photoneutrons KAERI01u, LA150u, and CNDC01u libraries were also used. For electron, photon, and neutron, the default physics cards were used unless in the PHYS: N card the maximum energy of neutrons set to 40 MeV for variance reduction and the fourth entry at PHYS: P card set to 1 to reduce the relative statistical uncertainty and allow photoneutrons production interactions.

Neutron source strength (Q_n), was calculated based on McGinley and Landry method.^[10] First, a sphere, with center at the target and radius of 100 cm, was considered, then the number of passed neutrons was calculated using F1 tally on the surface of the sphere, with closed collimator jaws. The code computes tallies for one electron of the source. For comparing the results with findings of others, output was derived in terms of 1 Gy of photon dose in the water phantom at “depth of maximum absorbed dose” (d_{max}). Hence, the

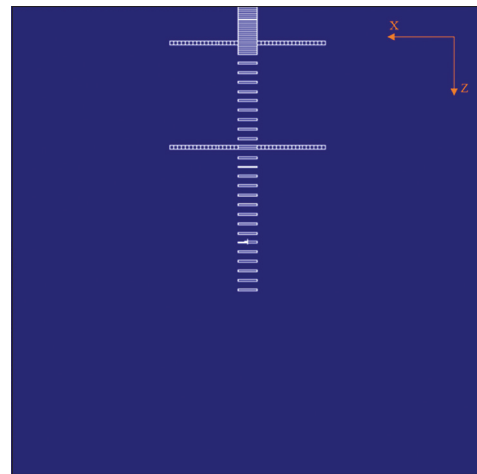


Figure 3: Side view of simulated water phantom. The voxels along Z axis used for calculation of percentage depth dose and the voxels along X axis used for dose profile

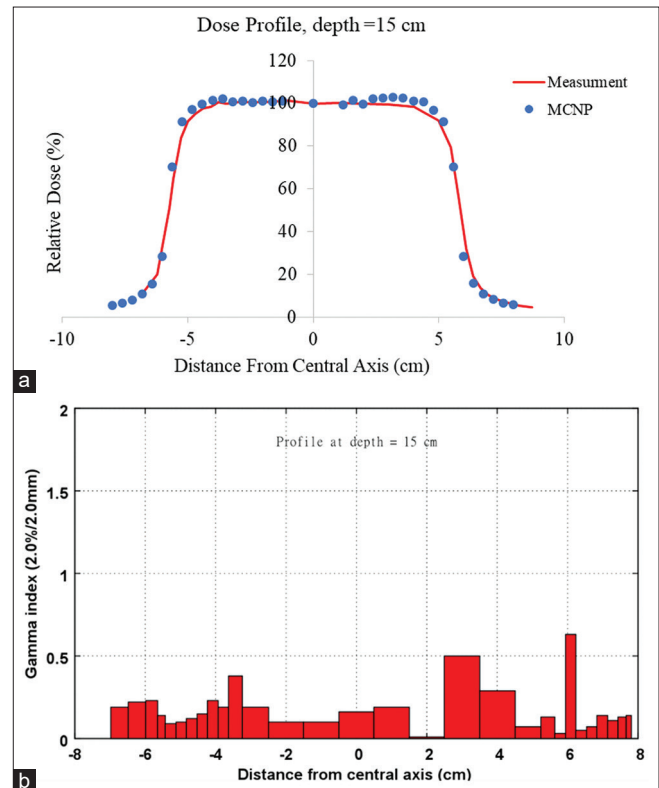


Figure 5: (a) Dose profiles in water phantom were determined by measurement and calculation at depth 15 cm, (b) gamma index values for comparing measurement with and calculation

number of required electrons for delivering 1 Gy of photon dose at d_{max} was derived and multiplied with the outputs of the code. Accordingly, the neutron source strength obtained in terms of n/Gy.

The fluence of photoneutrons was calculated using F4 tally in terms of neutrons/cm²/electron and converted to n/cm²/Gy unit.

DE obtained by F4 tally and fluence-to-DE coefficients. These coefficients derived from NCRP No. 38 and exerted using “dose energy” and “dose function” cards. Unit of this quantity converted to mSv/Gy.

Kerma acquired using F6 tally in terms of MeV/g/electron, which changed to mGy/Gy.

RESULTS

In Figures 5, 6 and 7 results of measurements and calculations for PDD and dose profile were compared with each other. Uncertainty of calculated doses was often $<1\%$. For evaluating the agreement between calculated and measured results, the gamma index values were derived for criteria of 2 mm for “distance to agreement” and 2% for “dose difference.” In all points, the values of the gamma index were less than unity. Gamma index <1 means the existence of an acceptable agreement between simulation and measurement. Hence, the accuracy of the simulation was verified.

The number of required electrons for delivering 1 Gy of photon dose in the water phantom at d_{\max} , was calculated. This number was depicted by N_e in Table 1. An important quantity, which demonstrates the ability of each Linac for producing photoneutrons, was the neutron source strength. The maximum fluence of photoneutrons on the beam axis (Φ_{\max}) with related and the corresponding depths was shown in this table. As it is obvious from Table 1, our results were in agreement with

published data and validate the simulation for photoneutron calculations as well

Figure 8 shows the fluence of thermal, epithermal, fast and total photoneutrons along the central axis as well as transverse direction at depths of 0.1, 1, 2, 10, and 20 cm of the phantom. Results of Kry *et al.*^[19] and Martínez-Ovalle *et al.*^[18] (i. e., with the same type of Linac, energy, phantom, field size, and SSD) for total photoneutrons were depicted on Figure 8a and shows agreement between our calculations and these data.

Figure 9 shows the fluence of thermal, epithermal, fast and total photoneutrons in transvers direction at depths of 0.1, 1, 2, 10 and 20 cm of the phantom

Figure 10 shows DE of thermal, epithermal, fast, and total photoneutrons in transverse direction at depths of 0.1, 1, 2, 10, and 20 cm of the phantom. Calculations of Kry *et al.*^[19] (i. e., with the same type of Linac, energy, phantom, field size, and SSD) for total photoneutrons are depicted in Figure 10d that were consistent with this research

Figure 11 shows kerma of thermal, epithermal, fast, and total photoneutrons in transverse direction at depths of 0.1, 1, 2, 10, and 20 cm of the phantom

DISCUSSION

Figure 8 shows fluence, DE and kerma of photoneutrons on the central axis of the treatment photon beam. In Figure 8a, the

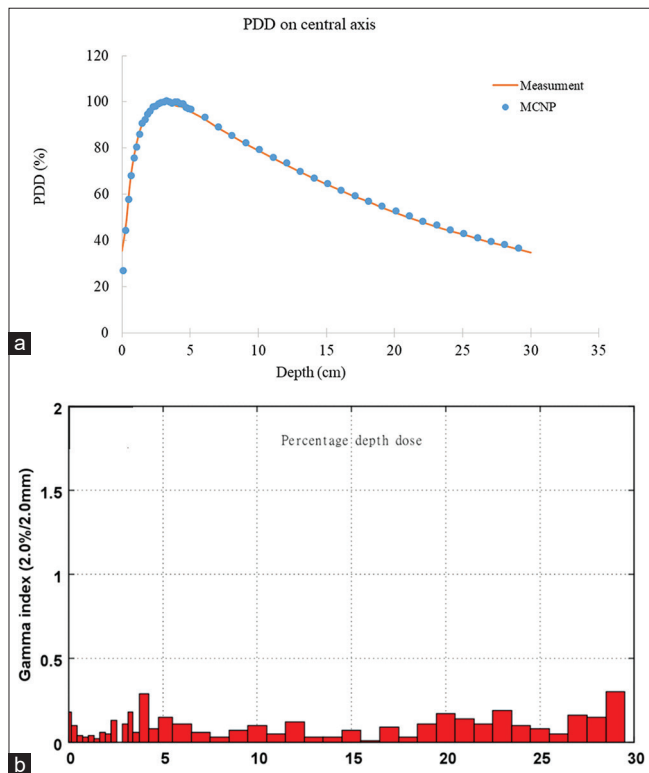


Figure 6: (a) Percentage depth doses in water phantom were determined by measurement and calculation, (b) Gamma index values for comparing the differences between measurement and with calculation

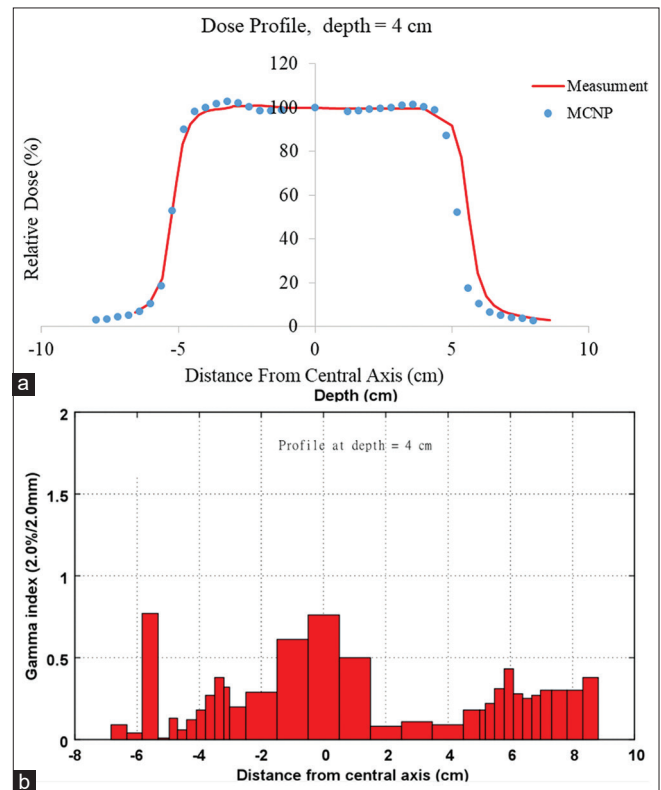


Figure 7: (a) Dose profiles in water were determined by measurement and calculation at depth of 4 cm, (b) gamma index values for comparing measurement and with calculation.

Table 1: Required electrons for delivering 1 Gy of photon dose (N_e), neutron source strength (Q_n), maximum fluence of photoneutrons on the beam axis (Φ_{max}) and depth of maximum fluence of photoneutrons ($d_{\Phi_{max}}$) for Varian 2100 C/D Linac operated at 18 MV in a number of studies

Authors	N_e (10^5 electrons/Gy)	Q_n (10^{12} n/Gy)	Φ_{max} (10^{-8} n cm^{-2} / electrons)	$d_{\Phi_{max}}$ (cm)
Mesbahi <i>et al.</i> ^[29]	–	1.3	–	–
Martínez-Ovalle <i>et al.</i> ^[18]	–	–	3.25	2.03
Chegeni <i>et al.</i> ^[28]	1.26	1.38	–	–
This work	1.28	1.37	3.42	2

Table 2: Fluence, dose equivalent and kerma of total photoneutrons on central axis of the treatment beam in the phantom

Dosimetry quantity	d_{max} (cm)	Maximum	ADA	(ADA/maximum) \times 100
Fluence	2	43.8 n/cm ² /Gy	3.89 n/cm ² /Gy	9%
DE	0.1	0.26 mSv/Gy	0.004 mSv/Gy	2%
Kerma	0.1	3.62 mGy/Gy	0.08 mGy/Gy	2%

d_{max} : Depth of maximum quantity, ADA: Average in deep area. DE: Dose equivalent

Table 3: Average fluence of total photoneutrons in inner and outer areas at different depths and corresponding relative values

Depth (cm)	AIA (n/cm ² /Gy)	AOA (n/cm ² /Gy)	(AOA/AIA) \times 100
0.1	28.7	21.1	74%
1	37.4	26.1	70%
2	40.3	26.9	67%
10	15.2	10.0	66%
20	2.8	2.3	82%

Average at all depths 72%

AIA: Average in inner area, AOA: Average in outer area

findings of Kry *et al.*^[19] and Martínez-Ovalle *et al.*^[18] are also displayed. Since, in the study of Kry *et al.*,^[19] the parameters were in terms of an arbitrary unit, Martínez-Ovalle *et al.*^[18] multiplied them by 1.28 to fit the peaks of the curves. After depth of 15 cm Martínez-Ovalle *et al.*^[18]'s curve shows a little difference with both Kry *et al.*^[19]'s study and ours. Ignoring the role of walls, was the mean reason for continuing decline after the depth of 15 cm in this graph. It has been shown, if we ignore the walls of the treatment room, the fluence of thermal photoneutrons at isocenter will be estimated less than the actual amount.^[22] Therefore, the total fluence will be underestimated too. Martínez-Ovalle *et al.*,^[18] have attributed this effect to the existence of couch and backscattering of photoneutrons from it, that noted in Kry *et al.*^[19]'s simulation, however; we think it is because of ignoring the walls, since; we did not consider the couch and observed the same behavior. According to the Figure 8 effect of walls is negligible. Fluence of total photoneutrons on the central axis reached to its maximum value at depth 2 cm and then declined rapidly. Fast photoneutrons after entering the phantom, due to elastic interaction with Hydrogen nuclei and also elastic and inelastic interactions

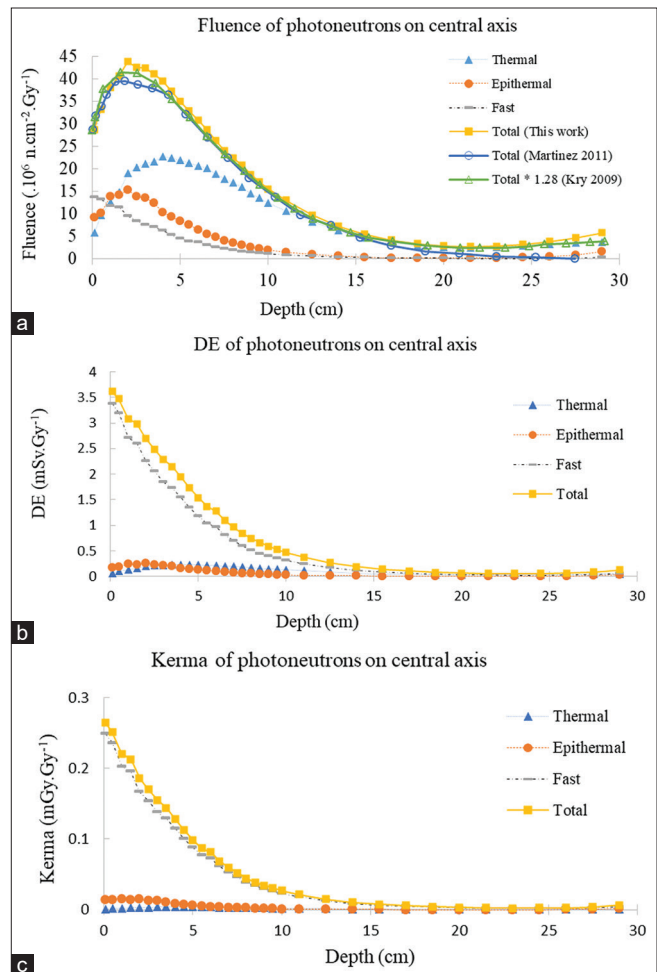


Figure 8: Fluence (a), dose equivalent (b), and kerma (c) of photoneutrons along central axis of the 18 MV photon treatment beam and 10 cm \times 10 cm radiation field in the ICRU phantom. For comparison the results of Martínez-Ovalle *et al.*^[18] and Kry *et al.*^[19] were also depicted (a)

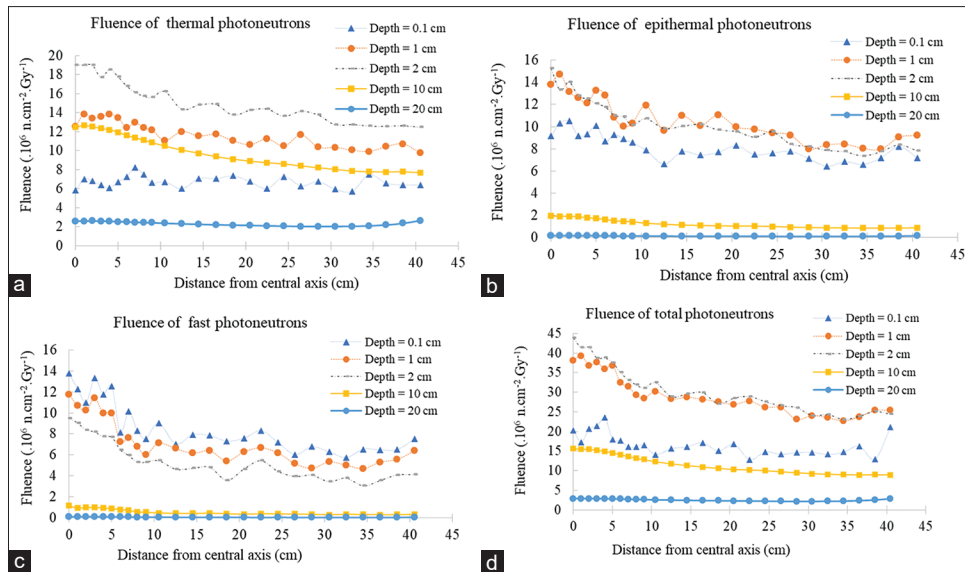


Figure 9: Fluence of thermal (a), epithermal (b), fast (c) and total (d) photoneutrons at transvers direction of the 18 MV photon treatment beam for $10\text{ cm} \times 10\text{ cm}$ radiation field at different depths in the ICRU phantom

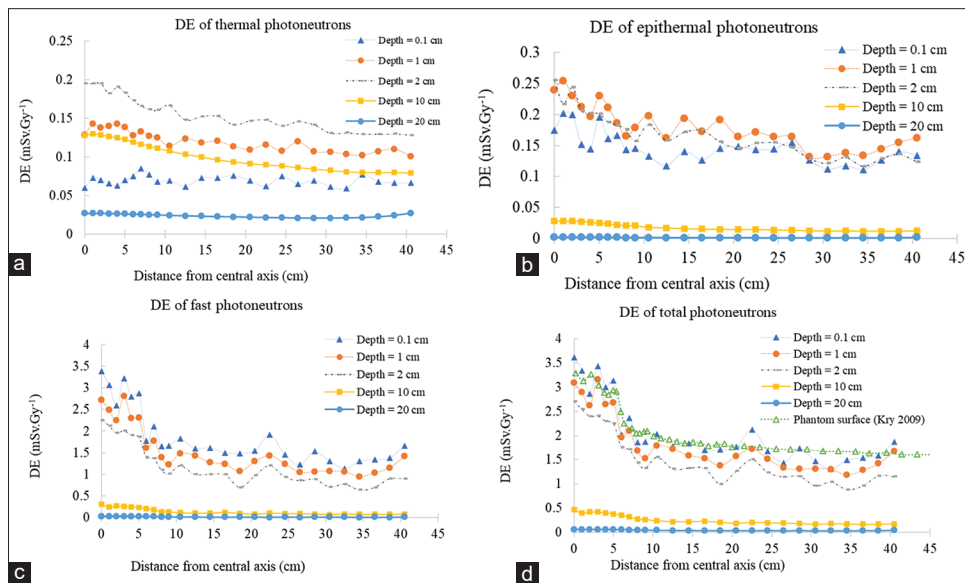


Figure 10: Dose equivalent of thermal (a), epithermal (b), fast (c) and total (d) photoneutrons at transvers direction of the 18 MV photon treatment beam and $10\text{ cm} \times 10\text{ cm}$ radiation field at different depths in the ICRU phantom. For comparison the results of Kry *et al.*^[19] in the same situation were also depicted (d)

with other nuclei, gradually lose their energy and the number of thermal photoneutrons increase up to the depth of 4 cm then decrease rapidly because their capture cross-section will increase [Figure 12].^[30] Due to the large number of Hydrogen nuclei relative to Nitrogen nuclei,^[31] these nuclei have dominant role in the absorption of neutrons. From Figures 8 and 9, it could be observed that the fluence of thermal photoneutrons at depths more than about 1 cm was greater than epithermal and fast photoneutrons in all points of the phantom. DE and kerma had their maximum at the surface layer of the phantom (i.e. depth 0.1 cm) and rapidly reduce until the depth of 15 cm and after that remain nearly constant. Therefore,

we can divide the thickness of the phantom into two areas: Shallow area (i.e. depths <15 cm) and deep area (i.e. depths more than 15 cm). In Table 2 average of fluence, DE and kerma of total photoneutrons at deep area were compared with their maximums. From data of Figure 8b, it could be found out that from the surface of the phantom to the depth of 5 cm the DE of fast photoneutrons was one order of magnitude greater than values related to thermal photoneutrons and at depths more than 5 cm their order of magnitudes were the same. From Figure 8c we can result that from surface of the phantom to depth of 5 cm the kerma of fast photoneutrons was two order of magnitude greater than values related to thermal

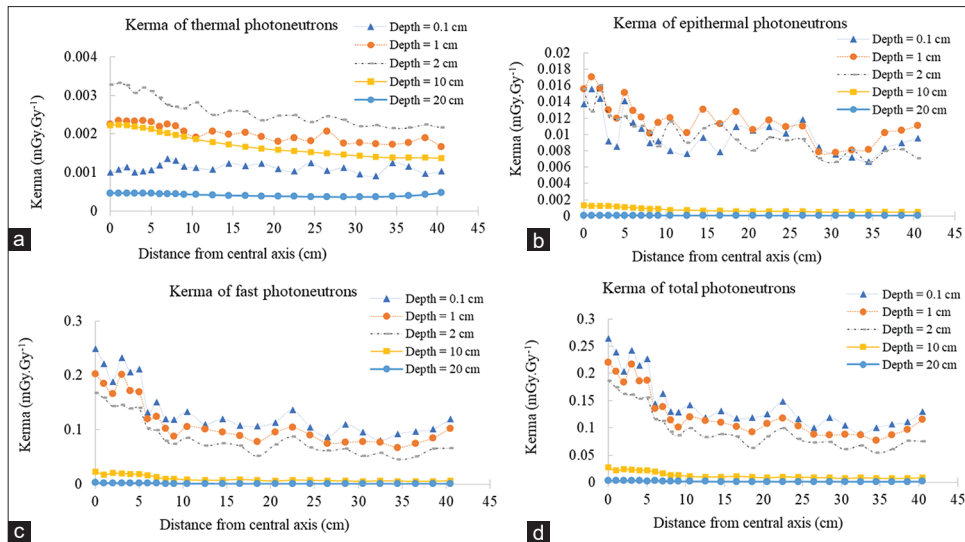


Figure 11: Kerma of thermal (a), epithermal (b), fast (c) and total (d) photoneutrons at transvers direction of the 18 MV photon treatment beam and 10 cm × 10 cm radiation field at different depths in the ICRU phantom.

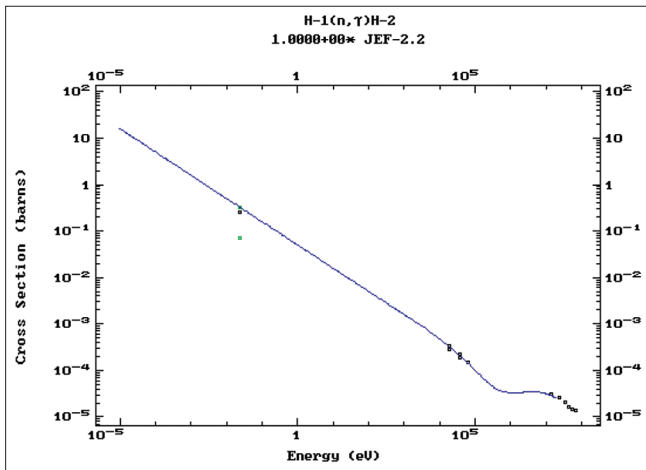


Figure 12: Thermal neutron capture cross section with hydrogen nucleus

photoneutrons and at depths more than 5 cm this ratio was one order of magnitude.

Figure 9 shows the Fluence of thermal, epithermal, fast, and total photoneutrons at transverse direction. Attention to these graphs indicates that fluence within the photon beam and lateral distances more than 10 cm for each group of photoneutrons, at all depths, were almost invariable and gradually decrease between these two areas. So, we can consider the phantom in the lateral direction in three areas: Inner area of photon treatment beam (i.e. transverse distances less than 5 cm), photoneutron’s penumbra area (i.e. transverse distances between 5 cm and 10 cm) and outer area (i.e. transverse distances more than 10 cm). In Table 3, as a sample, average of total photoneutrons at the inner area and outer area in different depths were compared. The average fluence at the outer area was less than the inner area and in the whole was about 72%. This comparison could be carried out for thermal, epithermal, and fast photoneutrons

Table 4: Average DE of total photoneutrons in inner and outer areas at different depths and corresponding relative values

Depth (cm)	AIA (mSv/Gy)	AOA (mSv/Gy)	(AOA/AIA) × 100
0.1	3.23	1.69	52%
1	2.85	1.48	52%
2	2.43	1.19	49%
10	0.41	0.20	47%
20	0.059	0.036	60%

Average at all depths 52%

AIA: Average in inner area, AOA: Average in outer area

Table 5: Average kerma of total photoneutrons in inner and outer areas at different depths and corresponding relative values

Depth (cm)	AIA (mGy/Gy)	AOA (mGy/Gy)	(AOA/AIA) × 100
0.1	0.23	0.12	51%
1	0.20	0.10	50%
2	0.17	0.08	46%
10	0.023	0.009	38%
20	0.003	0.001	42%

Average at all depths 45%

AIA: Average in inner area, AOA: Average in outer area

separately, too. At each depth, fluence of thermal, epithermal, and fast photoneutrons had the same order of magnitude.

Figure 10 shows DE of thermal, epithermal, fast, and total photoneutrons at transverse direction. In Table 4, as a sample, the average DE of total photoneutrons at the inner area and outer area in different depths have been compared with each other. The average of DE at the outer area was less than the inner area,

especially for fast photoneutrons, and in whole, was about 52% of its inner value. At shallow area, DE of fast photoneutrons was one order of magnitude larger than thermal and epithermal photoneutrons, but in deep area, all three categories had the same order of magnitude

Figure 11 shows kerma of thermal, epithermal, fast, and total photoneutrons at transverse direction. In Table 5, as a sample, the average kerma of total photoneutrons in inner and outer areas at different depths have been compared with each other. Average of kerma in the outer area was less than the inner area, especially for fast photoneutrons, and in whole was about 45% of its inner value. At shallow area, kerma of fast photoneutrons was two order of magnitude larger than thermal photoneutrons

CONCLUSION

In ICRU soft-tissue phantom, variation of fluence, DE and kerma in transverse direction were mild, and along the central axis at the shallow area were sharp. At any depth, average of fluence, DE and kerma in the outer area of the field were less than the inner area and in general were about 72%, 52%, and 45%, respectively. Fluence of thermal photoneutrons at all points, except at depths <1 cm, was more than other categories of photoneutrons and their order of magnitudes were the same. DE of fast photoneutrons at shallow area was one order of magnitude greater than thermal photoneutrons, and for deep area had the same order. At shallow area, kerma of fast photoneutrons was two order of magnitude larger than thermal photoneutrons.

Acknowledgment

The authors would like to greatly thank Dr. S. R. Mahdavi (Medical College, Iran Medical Sciences University, Tehran, Iran) for his valuable guidance on conducting the process of accuracy verification of the applied code.

Financial support and sponsorship

Nil.

Conflicts of interest

There are no conflicts of interest.

REFERENCES

- Alfuraih A, Chin M, Spyrou N. Measurements of the photonuclear neutron yield of 15 MV medical linear accelerator. *J Radioanal Nucl Chem* 2008;278:681-4.
- Siebert B, Schuhmacher H. Radiation Protection Dosimetry Quality factors, ambient and personal dose equivalent for neutrons, based on the new ICRU stopping power data for protons and alpha particles. *Radiat Prot Dosim* 1995;58:177-83.
- Israngkul-Na-Ayuthaya I, Suriyapee S, Pengvanich P. Evaluation of equivalent dose from neutrons and activation products from a 15-MV X-ray LINAC. *J Radiat Res* 2015;56:919-26.
- Karimi AH, Vega-Carrillo HR. Grid therapy vs. conventional radiotherapy – 18 MV treatments: Photoneutron contamination along the maze of a linac bunker. *Appl Radiat Isot* 2020;158:109064.
- Hosseinzadeh E, Banaee N, Nedaie HA. Monte Carlo calculation of photo-neutron dose produced by circular cones at 18 MV photon beams. *Rep Pract Oncol Radiother* 2018;23:39-46.
- Ghasemi A, Pourfallah TA, Akbari MR, Babapour H, Shahidi M. Photo neutron dose equivalent rate in 15 MV X-ray Beam from a Siemens Primus Linac. *J Med Phys* 2015;40:90-4.
- Waller EJ, Jamieson TJ, Cole D, Cousins T, Jammal RB. Experimental and computational determination of neutron dose equivalent around radiotherapy accelerators. *Radiat Prot Dosimetry* 2003;107:225-32.
- Lin JP, Chu TC, Lin SY, Liu MT. The measurement of photoneutrons in the vicinity of a Siemens Primus linear accelerator. *Appl Radiat Isot* 2001;55:315-21.
- Lee JH, Hwang WS, Chiu CH, Chen WL. Dose equivalent measurement in the vicinity of a medical linear accelerator. *Nucl Sci J Taipei* 1998;35:182-7.
- McGinley PH, Landry J. Neutron contamination of x-ray beams produced by the varian clinac 1800. *Phys Med Biol* 1989;34:777.
- Bezack E, Takam R, Marcu LG. Peripheral photon and neutron doses from prostate cancer external beam irradiation. *Radiat Prot Dosimetry* 2015;167:591-601.
- Bezack E, Takam R, Yeoh E, Marcu LG. The risk of second primary cancers due to peripheral photon and neutron doses received during prostate cancer external beam radiation therapy. *Phys Med* 2017;42:253-8.
- Sohrabi M, Hakimi A. Novel air-to-tissue conversion factors for fast, epithermal and thermal photoneutrons in a siemens ONCOR dual energy 18 MV X-ray medical linear accelerator. *Radiat Meas* 2019;126:106138.
- Bagheri H, Rabie Mahdavi S, Shekarchi B, Manouchehri F, Farhood B. Measurement of the contralateral breast photon and thermal neutron doses in breast cancer radiotherapy: A comparison between physical and dynamic wedges. *Radiat Prot Dosimetry* 2018;178:73-81.
- Bagheri H, Abedi Firouzjah R, Farhood B. Measurement of the photon and thermal neutron doses of contralateral breast surface in breast cancer radiotherapy. *J Radiother Pract* 2019;9:1-7.
- Barquero R, Mendez R, Vega-Carrillo HR, Iñiguez MP, Edwards TM. Neutron spectra and dosimetric features around an 18 mv linac accelerator. *Health Phys* 2005;88:48-58.
- Alem-Bezoubiri A, Bezoubiri F, Badreddine A, Mazrou H, Lounis-Mokrani Z. Monte Carlo estimation of photoneutrons spectra and dose equivalent around an 18 MV medical linear accelerator. *Radiat Phys Chem* 2014;97:381-92.
- Martínez-Ovalle SA, Barquero R, Gómez-Ros JM, Lallena AM. Neutron dose equivalent and neutron spectra in tissue for clinical linacs operating at 15, 18 and 20 MV. *Radiat Prot Dosimetry* 2011;147:498-511.
- Kry SF, Howell RM, Salehpour M, Followill DS. Neutron spectra and dose equivalents calculated in tissue for high-energy radiation therapy. *Med Phys* 2009;36:1244-50.
- Kry SF, Titt U, Followill D, Pönisch F, Vassiliev ON, White RA, *et al.* A Monte Carlo model for out-of-field dose calculation from high-energy photon therapy. *Med Phys* 2007;34:3489-99.
- Kry SF, Titt U, Pönisch F, Followill D, Vassiliev ON, White RA, *et al.* A Monte Carlo model for calculating out-of-field dose from a varian 6 MV beam. *Med Phys* 2006;33:4405-13.
- Mohammadi N, Miri-Hakimabad H, Rafat-Motavalli L, Akbari F, Abdollahi S. Patient-specific voxel phantom dosimetry during the prostate treatment with high-energy linac. *J Radioanal Nucl Chem* 2015;304:785-92.
- Abou-Taleb WM, Hassan MH, El Mallah EA, Kotb SM. MCNP5 evaluation of photoneutron production from the Alexandria University 15 MV Elekta Precise medical LINAC. *Appl Radiat Isot* 2018;135:184-91.
- Bahreyni Toossi MT, Behmadi M, Ghorbani M, Gholamhosseinian H. A Monte Carlo study on electron and neutron contamination caused by the presence of hip prosthesis in photon mode of a 15 MV Siemens PRIMUS linac. *J Appl Clin Med Phys* 2013;14:52-67.
- Ghassoun J, Senhou N. The evaluation of neutron and gamma ray dose equivalent distributions in patients and the effectiveness of shield materials for high energy photons radiotherapy facilities. *Appl Radiat Isot* 2012;70:620-4.
- Rezaian A, Nedaie HA, Banaee N. Measurement of neutron dose in the compensator IMRT treatment. *Appl Radiat Isot* 2017;128:136-41.
- Ghorbani M, Azizi M, Azadegan B, Mowlavi AA, Rahvar ZA, Wagner W. Dosimetric evaluation of neutron contamination caused by dental restorations during photon radiotherapy with a 15 MV Siemens

- Primus linear accelerator. *Radiat Phys Chem* 2020;174:108961.
28. Chegeni N, Karimi AH, Jabbari I, Arvandi S. Photoneutron dose estimation in GRID therapy using an anthropomorphic phantom: A Monte Carlo study. *J Med Signals Sens* 2018;8:175-83.
 29. Mesbahi A, Ghiasi H, Mahdavi SR. Photoneutron and capture gamma dose equivalent for different room and maze layouts in radiation therapy. *Radiat Prot Dosimetry* 2010;140:242-9.
 30. Kopecky J, Sublet JC, Simpson J, Forrest R, Nierop D. Atlas of Neutron Capture Cross Sections. INDC(NDS)-362, Distrib.: G+AT, Austria: International Atomic Energy Agency; 1997.
 31. McConn RJ, Gesh CJ, Pagh RT, Rucker RA, Williams R 3rd. Compendium of Material Composition data for Radiation Transport Modeling. Richland, WA (United States): Pacific Northwest National Lab.(PNNL); 2011.